



Optimization of 4D Flow MRI Spatial and Temporal Resolution for Examining Complex Hemodynamics in the Carotid Artery Bifurcation

Retta El Sayed¹ · Alireza Sharifi² · Charlie C. Park² · Diogo C. Haussen³ · Jason W. Allen^{1,2,3} · John N. Oshinski^{1,2,3}

Received: 12 January 2023 / Accepted: 24 April 2023 / Published online: 8 May 2023
© The Author(s) under exclusive licence to Biomedical Engineering Society 2023

Abstract

Background Three-dimensional, ECG-gated, time-resolved, three-directional, velocity-encoded phase-contrast MRI (4D flow MRI) has been applied extensively to measure blood velocity in great vessels but has been much less used in diseased carotid arteries. Carotid artery webs (CaW) are non-inflammatory intraluminal shelf-like projections into the internal carotid artery (ICA) bulb that are associated with complex flow and cryptogenic stroke.

Purpose Optimize 4D flow MRI for measuring the velocity field of complex flow in the carotid artery bifurcation model that contains a CaW.

Methods A 3D printed phantom model created from computed tomography angiography (CTA) of a subject with CaW was placed in a pulsatile flow loop within the MRI scanner. 4D Flow MRI images of the phantom were acquired with five different spatial resolutions (0.50–2.00 mm³) and four different temporal resolutions (23–96 ms) and compared to a computational fluid dynamics (CFD) solution of the flow field as a reference. We examined four planes perpendicular to the vessel centerline, one in the common carotid artery (CCA) and three in the internal carotid artery (ICA) where complex flow was expected. At these four planes pixel-by-pixel velocity values, flow, and time average wall shear stress (TAWSS) were compared between 4D flow MRI and CFD.

Hypothesis An optimized 4D flow MRI protocol will provide a good correlation with CFD velocity and TAWSS values in areas of complex flow within a clinically feasible scan time (~ 10 min).

Results Spatial resolution affected the velocity values, time average flow, and TAWSS measurements. Qualitatively, a spatial resolution of 0.50 mm³ resulted in higher noise, while a lower spatial resolution of 1.50–2.00 mm³ did not adequately resolve the velocity profile. Isotropic spatial resolutions of 0.50–1.00 mm³ showed no significant difference in total flow compared to CFD. Pixel-by-pixel velocity correlation coefficients between 4D flow MRI and CFD were > 0.75 for 0.50–1.00 mm³ but were < 0.5 for 1.50 and 2.00 mm³. Regional TAWSS values determined from 4D flow MRI were generally lower than CFD and decreased at lower spatial resolutions (larger pixel sizes). TAWSS differences between 4D flow and CFD were not statistically significant at spatial resolutions of 0.50–1.00 mm³ but were different at 1.50 and 2.00 mm³. Differences in temporal resolution only affected the flow values when temporal resolution was > 48.4 ms; temporal resolution did not affect TAWSS values.

Conclusion A spatial resolution of 0.74–1.00 mm³ and a temporal resolution of 23–48 ms (1–2 k-space segments) provides a 4D flow MRI protocol capable of imaging velocity and TAWSS in regions of complex flow within the carotid bifurcation at a clinically acceptable scan time.

Keywords 4D flow MRI · Spatial resolution · Temporal resolution · Carotid web · Phantom model

Associate Editor Keefe B. Manning oversaw the review of this article.

✉ John N. Oshinski
jnoshin@emory.edu

Extended author information available on the last page of the article

Introduction

Three-dimensional (3D), cardiac-gated, phase contrast magnetic resonance imaging with 3D velocity encoding, or *4D flow MRI* is a technique for providing time-resolved volumetric acquisitions of blood velocity measurements

in-vivo [1, 2]. The advantage of 4D flow MRI over ultrasound Doppler or 2D cine phase-contrast MRI (2D PCMR) is that it provides a complete, time-resolved, 3D velocity field across the vascular domain of interest. Thus, 4D flow MRI can characterize the flow field in a similar manner to results from computational fluid dynamics (CFD) simulations, although 4D flow MRI has lower temporal and spatial resolution. These 3D time-resolved velocity measurements are the basis for the calculation of hemodynamic parameters associated with vessel wall remodeling and thrombus formation, such as wall shear stress (WSS) [3–7]. The accuracy of these hemodynamics parameters depends on the accuracy of the underlying velocity measurements. Therefore, it is important to determine the 4D flow MRI parameters that can accurately evaluate time-dependent velocity values in complex flow environments. Complex flow is defined herein as flow conditions where flow separation and adverse pressure gradients create regions of reverse flow, high vorticity and helicity, and regions of flow stagnation, but not necessarily turbulent flow.

4D flow MRI has been extensively employed for measuring blood velocity in large arteries such as the aorta, and several studies have been undertaken to optimize acquisition parameters and validate velocity measurements [7–11]. The studies that have examined the effect of 4D flow MRI spatial resolution on hemodynamic parameters in the aorta found that velocity and wall shear stress (WSS) values are sensitive to changes in spatial resolution [6, 12]. However, there is a paucity of published data on optimizing spatial and temporal resolution in smaller vessels such as the carotid arteries, especially in the presence of complex, disturbed flow [13–15]. The main issue affecting the optimization of 4D flow MRI is the tradeoff between signal-to-noise, spatial–temporal resolution, volumetric coverage, and scan time; shorter scans are required for clinical applications. One of the limitations that restrict the widespread use of 4D flow MRI in clinical settings is the tradeoff between image quality and scan time. Many institutions and IRB's have policies that require additional research sequences to add less than 5 min to the clinical scan time [16]. *Therefore, this study aims to provide recommended spatial and temporal parameters for use in imaging the carotid artery by conducting an optimization study a carotid artery web phantom model.*

Carotid artery webs (CaWs) are non-inflammatory intraluminal shelf-like projections into the internal carotid artery (ICA) bulb that are seen in up to 21.2% of patients with cryptogenic stroke [17–19]. CaWs produce complex flow patterns; therefore, a CaW geometry was chosen as an example of a carotid artery with complicated flow [20, 21]. Accurate and detailed in vivo measurements of velocity are nearly impossible to obtain, and accurate methods of measuring velocity cannot be done within the MRI scanner. Most in vitro model measurements using laser Doppler

anemometry (LDA) or particle image velocimetry (PIV) required physically oversized models examined in a separate laboratory flow environment. Anatomically sized models limitation includes difficulty collecting velocity data along the vessel wall due to the small size and laser sheet thickness [22–24]. Therefore, we chose to use CFD as the reference standard for this 4D flow MRI optimization study. The CFD simulation was based on the segmentation of the phantom geometry and an input mean velocity using a 2D PCMR in the common carotid artery. Voxel-to-voxel correlations of 4D flow MRI velocities with CFD velocities and regional correlations of 4D flow MRI WSS and CFD WSS were done at multiple locations in the CaW phantom geometry. *The objective of this study was to determine the 4D flow MRI spatial and temporal resolution parameters that produce accurate velocity and WSS measurements in regions of complex blood flow in the carotid artery within a clinically acceptable time frame.*

Materials and Methods

Phantom Models

The CaW model was segmented from a computed tomography angiography (CTA) scan of a patient with a CaW (Fig. 1a, b) (Spatial resolution: $0.49 \times 0.49 \times 0.63 \text{ mm}^3$). The segmentation was done using Mimics (Materialise NV, 2019), and the 3D model underwent smoothing and was converted to a mesh using 3-Matic (Materialise NV, 2019). The phantom model was then 3D printed (Object 30, Stratasys Ltd, MN, 2020, Printer resolution: 0.025 mm) using an MRI visible rigid material (RGD525, Stratasys Ltd, MN, 2020) to reduce noise in the wall of the model in the phase images compared to silicon models [25, 26]. The entire model was scaled up by 25% to avoid model wall breakage during the 3D printing process (CCA diameter $\sim 9 \text{ mm}$).

The model and flow system provided conditions that were physiologically and hemodynamically similar to those seen in vivo. Fluid viscosity (3.5 cP) was set to match blood with a 40:60 glycerin: water mixture solution as a blood mimicking agent [27]. The geometry and flow conditions resulted in Reynolds number ≈ 300 in the CCA. Pulsatile flow was applied at a simulated heart rate of 60 bpm using a custom-made pulsatile flow pump [28]. The flow pump was in the scanner control room and rigid tubing connected the flow pump to the phantom model in the MR room. The flow waveform was controlled using a LabVIEW interface that prescribed a carotid-specific flow waveform and provided a TTL trigger pulse to the scanner (Fig. 1c–f). The flow pump pulsatile flow waveform was acquired based on an average of patient-specific 2D PCMR velocity measurements in the common carotid artery ($n = 8$).

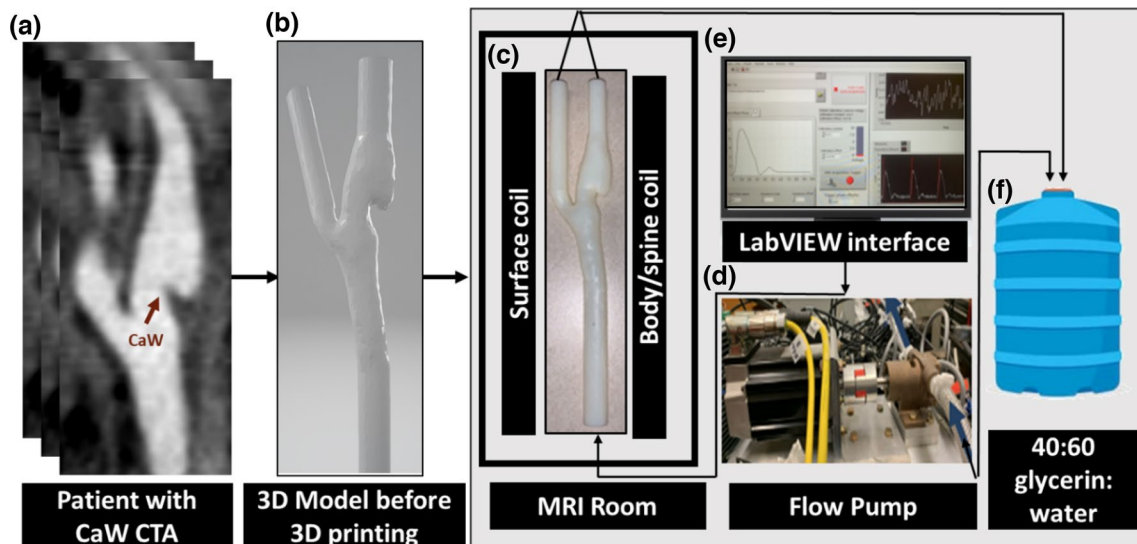


Fig. 1 Fabrication of the CaW Phantom Model. **a** The CTA images of a patient diagnosed with CaW (red arrow). **b** The 3D image (.stl file) of the segmented model from the CTA images. Highlighted in the gray background is an Overview of the flow system and phantom

model. **c** 3D printed phantom model placed in between the surface coil and body coil in a 3.0 T MRI scanner. **d** The in-house built pulsatile flow pump. **e** LabVIEW control interface for the flow pump. **f** Glycerin: Water fluid reservoir

MRI Studies

The phantom was placed in between a surface coil and a table-mounted spine coil element and imaged in a 3.0 Tesla MRI scanner (Siemens PrismaFit, Erlangen Germany). Multi-slab, transverse, 3D time of flight (TOF) images were acquired to cover the bifurcation (0.5 mm^3 , $\text{TR} = 23 \text{ ms}$, $\text{TE} = 3.1 \text{ ms}$). The 3D TOF scan provided the images to create geometry for the CFD simulation. 2D, ECG-gated, cine PCMR images were acquired 10 mm below and 10 mm above the bifurcation ($1 \times 1 \times 5 \text{ mm}^3$, $\text{VENC} = 80 \text{ cm/s}$, $\text{TR} = 43.6$, $\text{TE} = 7$). These 2D PCMR acquisition provided the flow values for the CFD simulations. Multiple 2D PCMR scans were acquired to monitor the flow pump performance throughout the scan session. 4D flow MRI scans were acquired in a parasagittal

orientation planned in the plane of the bifurcation with the following parameters: flip angle = 7° ; $\text{TE} \sim 5 \text{ ms}$; $\text{FOV} = 162 \times 200 \text{ mm}^2$, GRAPPA acceleration factor = 2, $\text{VENC} = 60 \text{ cm/s}$ in all directions. The matrix size was varied to change the spatial resolution. Because changing the spatial resolution changes the TE/TR, there was a range of temporal resolution for a given number of k-space lines in the MRI protocol settings. All spatial resolution tests were conducted using two k-space segments ranging the temporal resolution from (45.3–52.4 ms at different spatial resolutions). Temporal resolution was varied by changing the number of k-space segments per cardiac phase from one to four, which varied the temporal resolution from 23.2 to 92.7 ms acquired using 1 mm^3 isotropic spatial resolution. All images were retrospectively reconstructed with 24 timeframes over the cardiac cycle. Table 1 shows

Table 1 The different 4D flow MRI acquisition parameters investigated in this study, all acquisitions were retrospective (S: indicates the scans used for spatial resolution comparison, T: indicates the scans used for temporal resolution comparison, R: indicates the repeated scan for repeatability analysis)

Scan Number	TR/TE (ms)	Isotropic spatial resolution (mm^3)	Temporal resolution (ms)	Number of k-space segments	Scan time (min)
1 ^S	6.6/3.8	0.50	52.4	2	9:31
2 ^S	6.1/3.4	0.74	48.4	2	9:04
3 ^T	5.8/3.2	1.00	23.2	1	11:00
4 ^{S, T, R}	5.8/3.2	1.00	46.5	2	5:38
5 ^T	5.8/3.2	1.00	69.7	3	3:50
6 ^T	5.8/3.2	1.00	92.7	4	2:50
7 ^S	5.7/3.1	1.56	45.3	2	3:10
8 ^S	5.7/3.1	2.00	45.3	2	1:25

the list of 4D flow MRI scans acquired for this analysis. Clinically relevant scan time was specified as a scan time of ~ 10 min.

4D Flow MRI Processing

The 4D flow MRI data was analyzed using a custom-written MATLAB code and EnSight (ANSYS, Inc, PA, 2019) software [29]. A MATLAB program was used to correct for eddy currents and aliasing, perform noise filtering [30, 31], and calculate a 3D magnetic resonance angiogram (MRA) from the 4D flow MRI data as the mean of the sum of squares of the three-directional velocity encoding images. The carotid was segmented on the MRA and uploaded to EnSight for the visualization of velocity pathlines and the extraction of 2D time-resolved velocity values at specific locations (Fig. 2). Multiple 2D planes perpendicular to the centerline of the vessel were interrogated in the 3D geometry. These planes included: 10 mm below the bifurcation in the CCA, 10 mm, 15 mm, and 20 mm above the bifurcation in the ICA. The plane in the CCA was chosen as being representative of a laminar, nearly parabolic flow profile in a cylindrical tube [32]. While multiple planes in the ICA were chosen to evaluate flow in areas where complex flow was expected [32–34].

CFD Simulation

The geometric boundary conditions for the CFD simulation were created by segmenting the vessel lumen from 3D TOF MRA scans using Mimics. Segmenting the CFD geometry from the TOF images acquired at the same time as the 4D flow MRI scans assure the spatial registration of both geometries. The model was then loaded into 3-Matics for smoothing, adding extensions (10 times the diameter of the vessel), and meshing. Tetrahedral mesh for the CFD simulation was created in Fluent meshing mode, with multiple boundary layers to resolve near wall flow patterns with a 1.2 growth factor (Cells: 2,981,218, Faces: 7,295,963, Nodes: 1,374,872). Fluent (ANSYS, Inc) was used for solving 3D, time-resolved flow field using a finite volume implementation of a Navier–Stokes equation solver. The CFD simulation was conducted based on transient flow simulations using inlet mean velocity. A compiled user-defined function was applied at the inlet in fluent with a parabolic velocity profile (Fig. 2). The inlet flow boundary conditions were based on a 2D PCMR slice acquired perpendicular to CCA. 2D PCMR was used as a CFD inlet condition for the CFD simulation to be completely independent of the 4D flow measurements. For the outlet, constant pressure was applied with the assumption of rigid walls, no-slip conditions, and a fluid with a viscosity of 0.0035 kg/m/s and density of 1050 kg/m³.

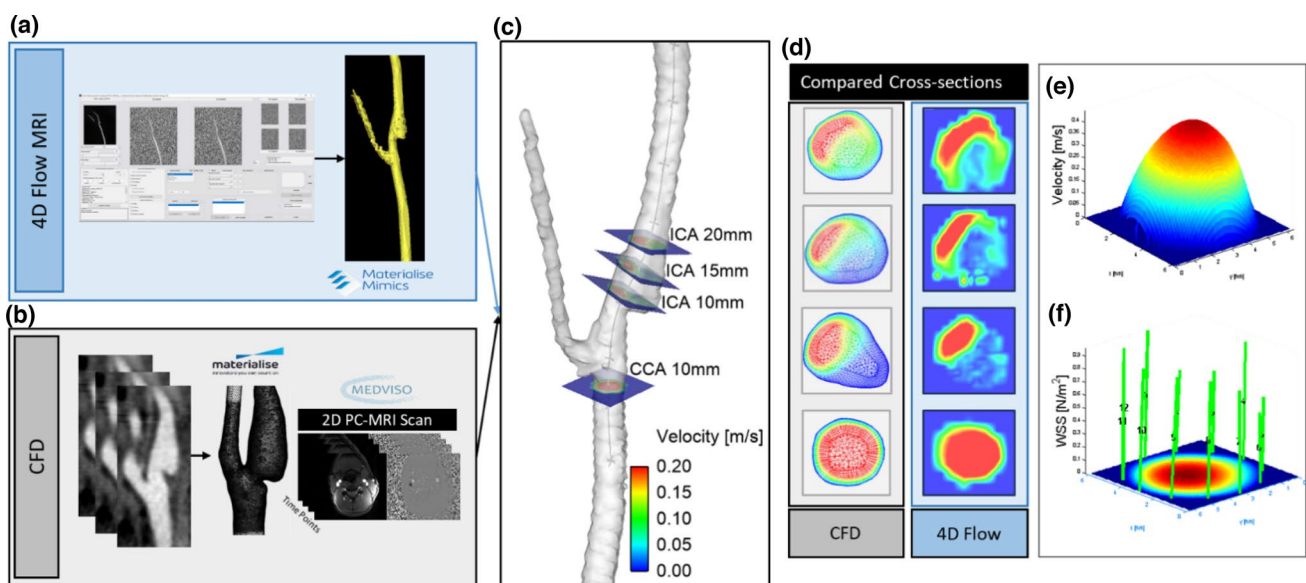


Fig. 2 Overview of 4D Flow and CFD processing methods. **a** 4D flow MRI methods (blue background) use the MATLAB base program for preprocessing the DICOM MRA images, materialize Mimics used for the segmentation, and EnSight for streamlines generation and 2D cross-section extraction. **b** CFD processing methods (gray background) geometry segmentation and smoothing using materialize mimics and 3-Matics, fluent for meshing and running CFD simula-

tions using inlet mean velocity waveform from PCMR data. **c** CFD and 4D flow MRI were compared at four cross-sections perpendicular to the vessel centerline. **d** 2D Cross-sections extracted: CCA 10 mm below the bifurcation, ICA 10 mm, ICA 15 mm, and ICA 20 mm above the bifurcation. **e** Velocity profile of a cross-section. **f** The WSS vectors at the twelve sectors across the corresponding cross-section

Comparison of 4D Flow MRI and CFD

4D flow MRI was compared to CFD at four cross-sectional locations: CCA 10 mm below bifurcation, and ICA 10 mm, 15 mm, and 20 mm above the bifurcation in the ICA (Fig. 2a–d). Both 4D flow MRI and CFD were loaded into EnSight and the cross-sections were inserted perpendicular to the centerline of the vessel, and velocity values of each cross-section were exported. EnSight was used for analyzing both 4D flow MRI and CFD and to ensure the registration of the two datasets. In 4D flow MRI, each cross-section was exported as a 64×64 matrix while in CFD the pixel size was dependent on the number of mesh elements in the geometry. Therefore, to match the resolution between 4D flow MRI data and CFD for voxel-to-voxel comparison, a MATLAB program was used to adjust the CFD to a matrix size of 64×64 having the same physical dimension as the 4D Flow MRI matrix. Additionally, the cross-sectional plane in the CCA was placed in the same location as the 2D PCMR slice placed 10 mm below the carotid bifurcation used as an inlet flow condition for the CFD. Therefore, the comparisons between the 2D PCMR 10 mm below the bifurcation (CFD inlet) and 4D Flow MRI in the CCA reflect comparisons at the same location.

Spatial Resolution Analysis

To evaluate the agreement of CFD and 4D flow MRI across different spatial and temporal resolutions, qualitative and quantitative analyses were done. For the qualitative analysis, the 3D axial velocity profile for four different cross-sections in the CCA and ICA of the phantom model based on 4D flow MRI scans at different spatial resolutions were visually compared to CFD. For the quantitative analysis, several hemodynamic parameters were quantified at each plane.

- *Voxel-to-voxel Pearson correlation for 4D flow MRI versus CFD* velocity values was performed at each time point over the cardiac cycle for all four cross-sectional planes. Bland Altman analysis was conducted for the cross-sectional plane in the ICA 10 mm above the bifurcation, as this is the location with the greatest amount of complex flow expected [32, 34].
- *Time Average Flow (TAF)* was quantified as the integral of the flow over the cardiac cycle over the vessel lumen at each location (ml/s), yielding a single number over the cardiac cycle. Standard deviation corresponds to the difference in flow rate values across the cardiac cycle. *The absolute difference in TAF between 4D flow MRI and CFD* was also determined across the four different cross-sections at different spatial resolutions. The final value of the absolute difference in TAF was represented as the average across the four cross-sectional plans, while the

standard deviation corresponds to the difference in TAF across the four cross-sectional planes.

- *Time Average Wall Shear Stress (TAWSS)* was calculated based on a previously published method in the literature [31, 35]. Briefly, WSS was derived based on the first-order derivative of velocity profiles using 4D flow MRI time-resolved images acquired and cubic b-spline interpolation [36, 37]. In-plane and axial WSS at all-time points at twelve sectors around the vessel wall boundary were extracted. TAWSS was then calculated in all twelve sectors across all 4D flow MRI scans and compared to CFD (Fig. 2f). TAWSS value represented an average of the TAWSS values across the twelve sectors and standard deviation represents the variation of the TAWSS in the vessel counter. *The absolute difference in TAWSS between 4D flow MRI and CFD* was also determined across the four different cross-sections at different spatial resolutions. The final value in the absolute difference in TAWSS between CFD and 4D flow MRI was calculated based on the average of TAWSS in the four cross-sectional planes, and the standard deviation represented the variation across the cross-sections.

Temporal Resolution Analysis

To evaluate the effect of changing temporal resolution on 4D flow MRI TAF, TAF absolute difference, TAWSS, and TAWSS absolute difference were calculated at the four different cross-sectional planes (CCA, 10 mm below the bifurcation, ICA 10 mm, ICA 15 mm, and ICA 20 mm above the bifurcation) in four different scans varying the temporal resolutions (23.2 ms, 46.5 ms, 69.7 ms, 92.7 ms) while keeping the spatial resolution constant at 1.00 mm^3 .

Repeatability Analysis

To understand the scan-rescan variations, a repeatability analysis was conducted. 4D flow MRI scans of isotropic spatial resolutions of 1.00 mm^3 and 46.5 ms temporal resolution were repeated two times during the scans, separated by one hour. These scans were analyzed as described above and TAF was reported at the four cross-sectional planes.

Statistical Analysis

The level of significance was 5%. All the results were presented as the mean \pm standard deviation. The voxel-to-voxel correlations were calculated as Pearson correlation coefficient where CFD and 4D flow MRI matrices were considered as two random variables and the correlation measured their linear dependency. For repeatability analysis, the velocity with the 24 timeframes during the cardiac cycle in the CCA plane in the two repeated measurements were

compared using ANOVA single Factor method. Bland–Altman analysis was conducted to understand the agreement between CFD and different 4D flow MRI scans in velocity, flow, and TAWSS. P-Values between CFD and 4D flow MRI were reported based on an independent Student's t-distribution. Linear regression analysis was conducted to understand the effect of spatial and temporal resolution on TAF measurements across different planes.

Results

Spatial Resolution Analysis

To understand the local differences of velocity at different spatial resolutions, a *qualitative* analysis was done using the 2D axial velocity profile for four different cross-sections in the CCA and ICA of the phantom model based on 4D flow MRI scans compared to CFD (Fig. 3). Qualitative spatial resolution analysis of 0.50 mm³ isotropic resolution showed the presence of noise in the measurements, including velocity values outside the vessel lumen. A resolution of 0.74 to 1.00 mm³ visually resolved complex flow patterns in CaWs within clinically reasonable scan time. An isotropic spatial

resolution of 1.50 and 2.00 mm³ spatially blurred out the skewing of the velocity profile.

To quantify the local point-by-point velocity profile differences, the voxel-to-voxel Pearson correlation coefficient was calculated between CFD and 4D flow MRI at every time point during the cardiac cycle for each of the four cross-sectional planes. Pearson correlation coefficient and Bland–Altman plot are shown for the ICA 10 mm cross-sectional plane in (Fig. 4). Spatial resolutions of 0.50, 0.74, and 1.00 mm³ resulted in a high level of correlation (> 0.75) to CFD (Fig. 4). The highest level of a voxel-to-voxel correlation coefficient is observed at an isotropic resolution of 0.74 mm³ of 0.87 ± 0.01. Resolution of 1.50 and 2.00 mm³ resulted in fair-to-poor correlation values of less than 0.50. The qualitative and quantitative spatial resolution results indicate that resolution values of 0.74–1.00 mm³ accurately capture the velocity profile values in the complex flow regions of the ICA in the presence of CaW.

The TAF values were summarized in Table 2 and were statistically different between 4D Flow MRI and CFD at a spatial resolution of 1.50 and 2.00 mm². The absolute difference of TAF between 4D Flow MRI and CFD was averaged over the four cross-sections for different spatial resolutions. Statistical analysis comparing the TAF absolute differences

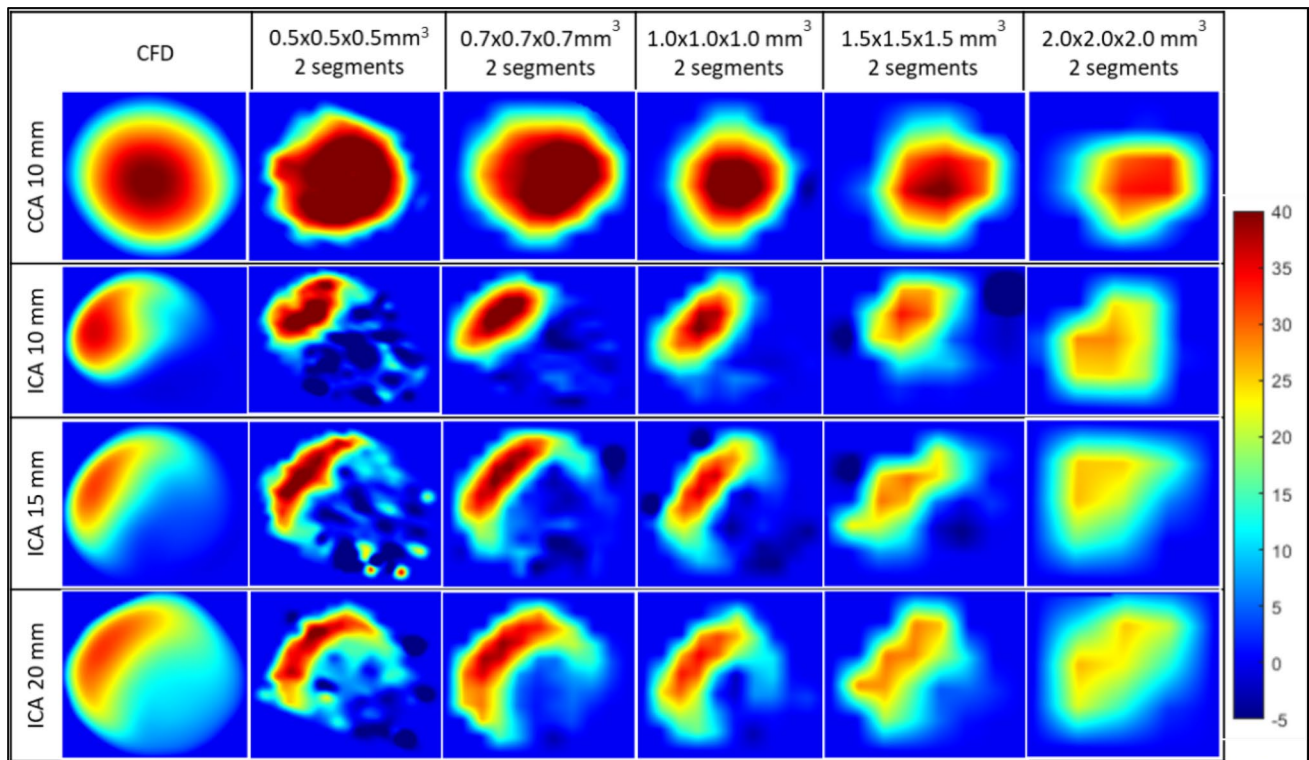


Fig. 3. 3D Axial velocity profile based on 4D flow MRI with different spatial resolutions compared to CFD simulations at four 2D planes: 10 mm below the carotid bifurcation in CCA, 10 mm, 15 mm, and 20 mm above the carotid bifurcation in the ICA. Note: the noise

increases in the velocity profile at higher spatial resolutions, while resolving the velocity profile, and skewing decreases at lower spatial resolutions

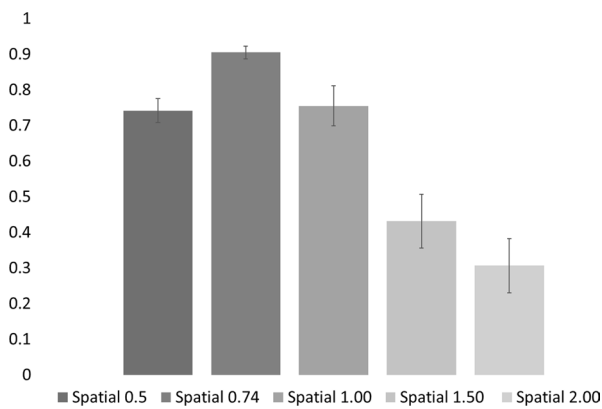


Fig. 4 Pearson correlation coefficients for voxel-to-voxel between 4D flow MRI and CFD at 10 mm distal to the bifurcation at different spatial resolutions. Correlation coefficients were calculated and averaged at different spatial resolutions and across all the time points in the cardiac cycle. All comparisons resulted in statistically significant values except for comparisons between resolutions of 1.00 vs. 0.5 and 1.50 vs. 2.00

showed that there was no statistical difference between spatial resolutions of 0.5, 0.74, and 1.00 mm³. Spatial resolutions of 1.50 and 2.00 mm³ were not statistically different from each other, but they were both statistically different from higher resolution values (0.5, 0.74, and 1.00 mm³) (Fig. 5a).

TAWSS values based on 4D flow MRI were calculated at four different planes and different spatial resolutions and compared to TAWSS values based on CFD. The absolute difference of TAWSS between 4D Flow MRI and CFD was averaged over the four cross-sections for different spatial resolutions (Fig. 5b). TAWSS calculated from 4D flow MRI

was lower than values calculated from CFD. An increase in the absolute difference is observed as spatial resolution decreases, the difference was 0.07 Pa and 0.13 Pa at 0.74 and 1.00 mm³, respectively. P-value and statistical analysis comparing TAWSS absolute differences between 4D flow MRI and CFD showed that there was no statistical difference between spatial resolutions of 0.5, 0.74, and 1.00 mm³. Spatial resolutions of 1.50 and 2.00 mm³ were not statistically different from each other, but they were both statistically different from higher resolution values (0.5, 0.74, and 1.00 mm³) (Fig. 5b), which was similar to what was seen in the absolute difference of TAF results. Table 3 shows the TAWSS averaged across the twelve sectors in each 4D flow MRI scan compared to CFD. Overall, the TAWSS based on 4D flow MRI are lower than CFD and they decrease as spatial resolution decrease.

Figure 6a-c shows a cross-section at 10 mm above the bifurcation comparing TAWSS between 4D flow MRI and CFD at different spatial resolutions on sector-based plots. Qualitatively, the results show an accurate representation of TAWSS distributions at different sectors when comparing 4D flow MRI values to CFD, but overall, 4D flow MRI values are lower. Figure 6d shows a Bland–Altman analysis of CFD vs 4D flow MRI at different spatial resolutions at the ICA 10 mm above the bifurcation, which align with the findings of the quantitative analysis. The results show an isotropic resolution between 0.74 mm³ provides the most accurate estimation of TAWSS compared to CFD.

Temporal Resolutions Analysis

TAF was analyzed at four cross-sections in four 4D Flow MRI scans with different temporal resolutions at 1.0 mm³

Table 2 TAF results at different spatial resolutions with the same temporal resolution (2 segments), four different temporal resolutions with the same isotropic spatial resolution of 1.00 mm³, and repeated scans at different plane locations across the phantom model compared to CFD

		Mean flow (ml/s)				
		Scan parameter	CCA 10 mm below bifurcation	ICA 10 mm above bifurcation	ICA 15 mm above bifurcation	ICA 20 mm above bifurcation
Spatial resolution	0.5		5.62 ± 0.84	4.49 ± 0.49*	4.61 ± 0.55	4.65 ± 0.59
	0.74		5.95 ± 0.82	5.03 ± 0.47	5.08 ± 0.46	4.81 ± 0.48
	1.00		5.70 ± 0.84	5.07 ± 0.66	4.97 ± 0.60	4.94 ± 0.48
	1.5		6.26 ± 0.91*	6.15 ± 0.59*	5.72 ± 0.74*	5.14 ± 0.52*
	2.00		6.39 ± 0.90*	7.56 ± 0.72*	6.32 ± 0.66*	5.58 ± 0.57*
Temporal resolution	Segment 1		6.13 ± 0.85	5.06 ± 0.56	5.14 ± 0.62*	5.06 ± 0.53
	Segment 2		5.70 ± 0.84	5.07 ± 0.66	4.97 ± 0.60	4.94 ± 0.48
	Segment 3		5.89 ± 0.78	5.29 ± 0.56*	5.24 ± 0.57*	5.33 ± 0.60*
	Segment 4		5.98 ± 0.75	5.30 ± 0.44*	5.23 ± 0.51*	5.29 ± 0.45*
Repeated scans	Scan 1		5.70 ± 0.84	5.07 ± 0.66	4.97 ± 0.60	4.94 ± 0.48
	Scan 2		5.77 ± 0.82	5.03 ± 0.58	5.08 ± 0.65	5.07 ± 0.53
CFD			5.83 ± 0.80	4.80 ± 0.55	4.80 ± 0.54	4.80 ± 0.54

Bold* indicates ($P \leq 0.05$) statistically significant based on unpaired t-test compared to CFD

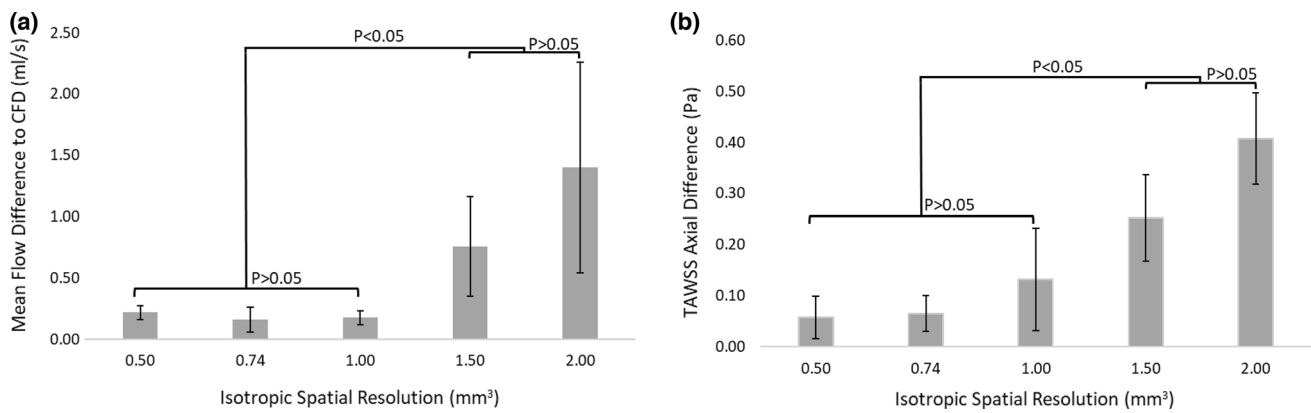


Fig. 5 **a** Absolute difference in mean flow between CFD and 4D flow MRI at different spatial resolutions averaged across the four different cross-sections. **b** Absolute difference in axial TAWSS between CFD and 4D flow MRI at different spatial resolutions averaged across the four different cross-sections. Statistical analysis: each pair were

compared using a T-Test unpaired two-sample equal variance. Note: looking at the figure and using an alpha critical value of 5%, the statistically insignificant p-value to different comparisons is displayed. Square brackets are showing statistical analysis between different comparisons

Table 3 TAWSS results averaged across the twelve sectors in each cross-section at different spatial resolutions with the same temporal resolution (2 segments), four different temporal resolutions with the same isotropic spatial resolution of 1.00 mm³, and repeated scans at different plane locations across the phantom model compared to CFD

		Mean axial TAWSS (P_a)			
		CCA 10 mm below bifurcation	ICA 10 mm above bifurcation	ICA 15 mm above bifurcation	ICA 20 mm above bifurcation
Spatial Resolution	0.5	0.92 ± 0.32	0.32 ± 0.32	0.42 ± 0.40	0.64 ± 0.37
	0.74	0.71 ± 0.20	0.33 ± 0.33	0.33 ± 0.27	0.60 ± 0.33
	1.00	0.79 ± 0.16	0.21 ± 0.21	0.36 ± 0.24	0.34 ± 0.25
	1.5	0.53 ± 0.22*	0.24 ± 0.23	0.22 ± 0.22	0.23 ± 0.21*
	2.00_1	0.33 ± 0.19*	0.11 ± 0.14*	0.06 ± 0.05*	0.10 ± 0.05*
Temporal Resolution	Segment 1	0.71 ± 0.21	0.20 ± 0.19	0.33 ± 0.19	0.33 ± 0.21*
	Segment 2	0.79 ± 0.16	0.21 ± 0.21	0.36 ± 0.24	0.34 ± 0.25
	Segment 3	0.76 ± 0.16	0.23 ± 0.21	0.36 ± 0.33	0.40 ± 0.21
	Segment 4	0.75 ± 0.14	0.25 ± 0.27	0.38 ± 0.32	0.40 ± 0.23
Repeated scans	Scan 1	0.79 ± 0.16	0.21 ± 0.21	0.36 ± 0.24	0.34 ± 0.25
	Scan2	0.78 ± 0.16	0.26 ± 0.31	0.34 ± 0.24	0.39 ± 0.22
CFD		0.80 ± 0.16	0.39 ± 0.44	0.43 ± 0.39	0.61 ± 0.42

Bold* indicates ($P \leq 0.05$) statistically significant based on unpaired t-test compared to CFD

isotropic resolution and compared to CFD. TAF in the CCA difference to CFD was found to be statistically insignificant at all the different temporal resolutions, but these results differ when complex flow patterns are present in the three ICA cross-sections (Table 2). Statistical analysis of the absolute difference of TAF showed insignificant difference with 1 segment and 2 segments (temp1), and at 3 segments and 4 segments (temp2), however, when comparing temp1 (1 or 2 segments) to temp2 (3 or 4 segments), p-value indicates a statistical difference (Fig. 7a). The temporal resolution results indicate that 1 or 2 segments capture the time-varying velocity values accurately for the carotid artery waveform.

Table 3 shows a limited effect on temporal resolution and TAWSS values. Figure 7b shows the results of the absolute difference between 4D flow MRI TAWSS and CFD, which indicates that temporal resolution does not affect TAWSS results. All comparisons resulted in P-values > 0.05 indicating statistically insignificant results.

Repeatability Analysis

We acquired the repeated scans at isotropic resolution 1.0 mm³, with a temporal resolution of 46.5 ms. TAF results at the CCA cross-section were 5.70 ± 0.84 and 5.77 ± 0.82 in

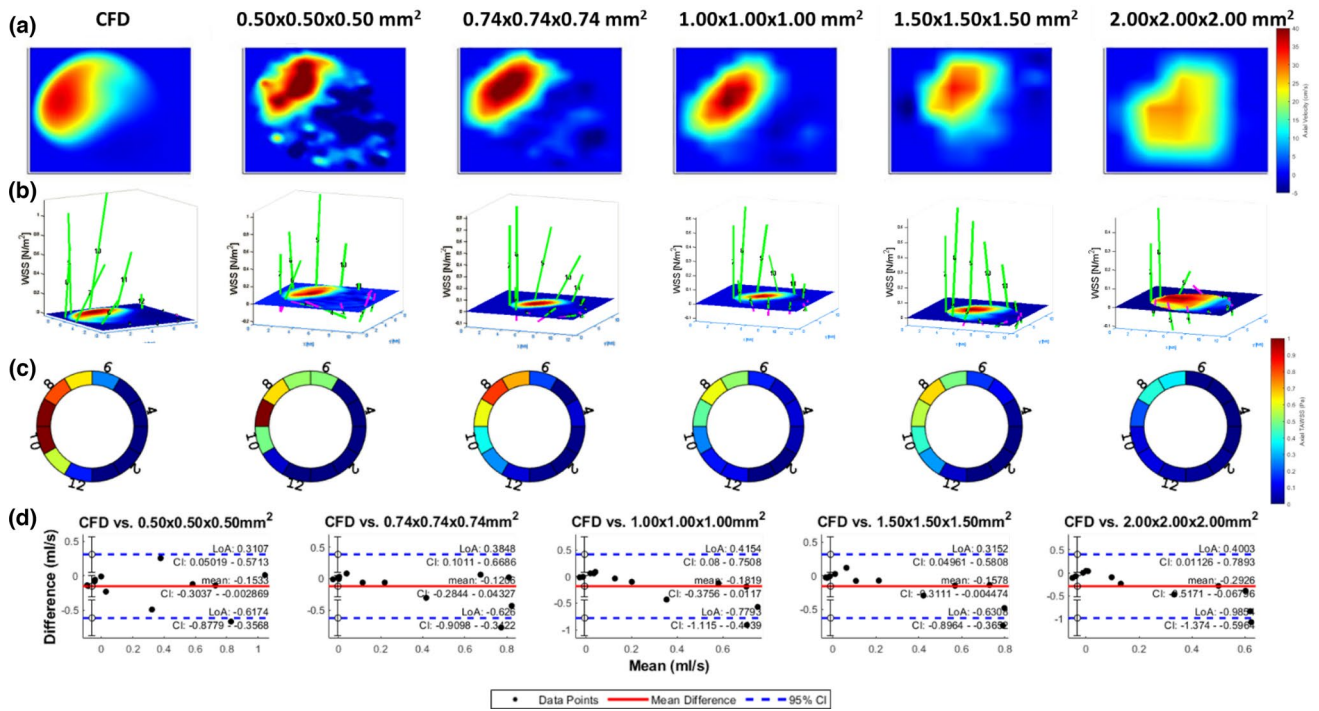


Fig. 6 TAWSS based on 4D flow MRI with different spatial resolutions compared to CFD simulations at 10 mm above the carotid bifurcation in the ICA. **a** shows the 3D axial velocity profile at peak systole. **b** shows the corresponding WSS vectors across the twelve sectors in the cross-section. **c** shows axial TAWSS heat maps corre-

sponded to each sector comparing different 4D flow MRI spatial resolutions to CFD. **d** shows the Bland–Altman analysis of CFD vs 4D flow MRI axial TAWSS across the twelve different sectors at different spatial resolution at 10 mm above the carotid bifurcation in the ICA

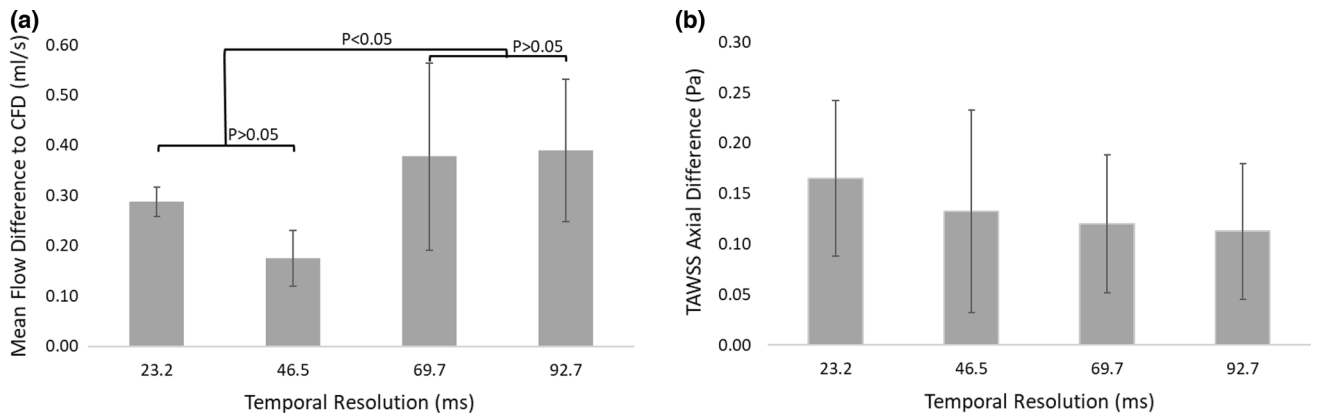


Fig. 7 a Compares the absolute difference in mean flow between CFD and 4D flow MRI at different temporal resolutions averaged across the four different cross-sections. **b** Compares the absolute difference in TAWSS axial between CFD and 4D flow MRI at different spatial resolutions averaged across the four different cross-sections. Statistical analysis: each pair were compared using a T-Test unpaired

two-sample equal variance. Note: looking at the figure and using an alpha critical value of 5%, the statistically insignificant p-value to different comparisons is shown in the figure. Box brackets show statistical analysis. In **b** all comparisons resulted in statistically insignificant analysis

the two scans, respectively (Table 2). ANOVA single factor analysis at the CCA cross-section (P-value = 0.76, F = 0.09), shows that ANOVA accepts the null hypothesis that both

scans' CCA flow means are equal the difference in repeated measurements was not statistically significant. TAWSS results were also repeatable (Table 3).

Discussion

The accuracy of 4D flow MRI-derived velocity measurements and WSS measurements in smaller vessels where complex disturbed flow is expected has not been well studied. We investigated 4D flow MRI using different spatial and temporal parameters and examined their effect on the accuracy of flow, velocity, and TAWSS measurements in a carotid artery bifurcation model based on a patient with a CaW. These parameter values can be applied in other studies using 4D flow MRI in smaller arteries such as the carotid. The major findings of this study are: (1) isotropic spatial resolution of 0.74–1.00 mm³ provides the best qualitative similarity to velocity profiles compared to CFD, the highest correlation coefficient of pixel-by-pixel velocity measurements between 4D flow MRI and CFD, and the lowest absolute difference in flow measurements between 4D flow MRI and CFD; (2) TAWSS derived from 4D flow MRI is generally lower than TAWSS from 4D Flow MRI, but the difference is only significant at lower spatial resolutions of 1.5–2.0 mm³; (3) Temporal resolution affects flow measurements, but to a lesser degree than spatial resolution, and temporal resolution does not affect TAWSS; (4) 4D Flow MRI results for flow are repeatable with statistically non-significant differences between multiple 4D Flow MRI scans and CFD.

Multiple studies have investigated the accuracy of velocity measurements acquired using MRI [6–11]. Harloff et al., have compared 4D flow MRI to ultrasound in healthy subjects and patients with $\geq 50\%$ stenosis in the carotid artery; the study found that 4D flow MRI significantly underestimated systolic blood flow and slightly overestimated it during diastole compared to ultrasound [38]. Other groups have looked at 4D flow MRI accuracy in a controlled setting. For example, the accuracy of 4D flow MRI had been investigated and compared to particle image velocimetry (PIV) in vitro carotid bifurcation model, where the root-mean-square error calculation showed errors values of 0.06 and 0.03 m/s when comparing 4D Flow MRI with stereoscopic PIV and tomographic PIV, respectively [39]. Montabla et al., used a thoracic aortic phantom to determine the variability of 4D flow MRI spatial and temporal resolution on peak flow, mean velocity, and stroke volume. They found high spatial resolution acquisitions are needed to determine reliable velocity profiles and WSS measurements which aligns with our findings [6]. Kweon et al., have compared 4D flow MRI spatial resolution accuracy on turbulent stenotic flow in a circular rigid phantom tube study (22 mm diameter) and the effect of 4D flow MRI spatial resolution (1, 1.5, and 3 mm) on flow rate, peak velocity, and flow patterns compared to flowmeter and CFD [12]. They found that the flow

rate in the stenosis region increased its fluctuations with increasing voxel size, whereas smaller error is observed proximal or distal to the stenotic region [12]. Similarly, we found that voxel size had little effect on the plane in the CCA, while higher errors were seen at larger voxel sizes in regions with complex flow patterns such as 10 mm distant to the bifurcation (Table 2).

Other studies have investigated the accuracy of 2D PCMR in determining the velocity profile and other hemodynamic metrics in phantom studies [4, 31, 40, 41]. Cibis et al., studied spatial and temporal resolution of 2D PCMR on the mean flow, peak flow, WSS, and oscillatory shear index using a carotid artery phantom [40]. They found a significant relationship between the mean flow and the spatial resolution (slope -13.0%/mm for the CCA) across a spatial resolution range of 0.2–1.00 mm³, without a significant correlation between the mean flow and temporal resolution. The results of our study found higher slope changes (34%/mm in CCA) across a larger spatial resolution range (0.50–2.0 mm³) compared to the Cibis et al. study [40]. Our results for TAWSS also agreed with Cibis et al. study, we found an approximately -24%/mm slope decrease of TAWSS results when decreasing spatial resolution in the CCA compared to -19%/mm in the Cibis study [40].

Many studies in the literature have described an underestimation of WSS measurements acquired using 4D flow MRI, which was also observed in this study [31, 40, 42–44]. The study results indicated a similar result where the values of TAWSS quantified by 4D flow MR scans compared to CFD were underestimated by 12%, 24%, 45%, and 73% at spatial resolutions of 0.74, 1.00, 1.50, and 2.00 mm³, respectively. One exception in this study was a spatial resolution of 0.5 mm³, where 4D flow MRI TAWSS values were slightly overestimated by 3% without a statistically significant difference. One reason that might have been the cause of this slight overestimation is the higher noise observed in the phase images at spatial resolution 0.5 mm³. Even though the phantom was 3D printed using an MRI visible material, we still observed some noise spikes (very high velocity values) near the wall that might have contributed to this slight overestimation.

We chose a phantom model with CaW since previous studies suggested complex flow patterns caused by its geometry [20, 45–47]. In patients with CaWs, the intraluminal shelf-like projection causes a flow acceleration on the proximal side of the web. On the distal side of the CaW, there is a sudden expansion in the lumen in many cases, which creates an unstable, separated, vortical flow pattern that gives rise to a large recirculation region, including stasis [20]. This sudden expansion will likely result in an extreme form of flow disturbance; therefore, we expect larger recirculation zones distal to a CaW shelf-like when compared to healthy

bulb anatomy. Low WSS is also expected just distal to the intraluminal carotid shelf, which is due to the large recirculation and blood stagnation region. Depending on the severity of the luminal narrowing, varying degrees of flow separation can cause stagnation regions that facilitate thrombosis formation [21, 47]. Individuals with disturbed flow patterns may be at higher risk of thrombosis and subsequent emboli leading to stroke/TIA due to this phenomenon [48]. Therefore, choosing the correct 4D flow MRI spatial and temporal resolution using a CaW phantom model will allow us to better evaluate complex flow patterns associated with CaW.

The study of carotid webs can be done with CFD in combination with CTA. The main advantage of 4D flow MRI over CFD is that 4D flow has the potential to provide the same 3D, time-resolved velocity field that CFD does, but immediately on the MRI scanner (with a ~5 min scan), therefore, 4D flow MRI provides significant clinical advantages over CFD. Although CFD is a very powerful tool it has its own set of limitations that prevented its implementation for clinical decision making [49]. CFD requires geometric information segmented from a medical imaging method such as CTA. Some of these limitations include the long processing time for CFD including segmentation, solution convergence, high computational power; and the need for multiple imaging modalities for obtaining accurate geometric and flow measurements [49].

Our study had several limitations. One limitation was that very high spatial and temporal resolution scans were not included. These scans required long scan times that are not practical for clinical use. Studies have found WSS is dependent on vessel wall segmentation, and WSS results can be dependent on segmentation [31, 40]. We did not evaluate different segmentation techniques, but all studies here were done by a single observer using the same methodology. Multiple methods can be used to calculate WSS, which by definition must use underlying velocity or flow values [35, 50, 51]. In this study, we evaluated TAWSS based on a method introduced in the literature previously, which has a limitation due to manual segmentation leading to user variability [36, 37]. Finally, the study observed limited changes to velocity and flow at different temporal resolutions, but we did not evaluate a full range of temporal resolution values for each spatial resolution. An analysis of particle residence time may be needed to fully understand temporal resolution effects in other hemodynamic parameters.

Conclusion

This study examined the effect of spatial and temporal resolution on measuring velocity, flow, and TAWSS with the aim of providing guidance for using 4D flow MRI in the carotid artery bifurcation in the setting of complex flow.

Qualitative analysis as well as quantitative analysis of voxel-to-voxel velocity correlation, time average flow, and TAWSS compared with CFD indicates that a spatial resolution of 0.74–1.00 mm³ and temporal resolution of 23–48 ms reflected by 1–2 k-space segments accurately determines velocity values accurately within a clinically reasonable scan time (isotropic 1 mm³ can be acquired in ~5 min). The velocity and flow measurements are more affected by variations in spatial resolution than the temporal resolution.

Acknowledgements The authors would like to acknowledge Paul Lee, Ph.D. at Emory University for the help in operating Object 30 3D printer.

Funding This work was funded by the American Heart Association Grant Nos. 0000065426 (Sharifi) and 19IPLOI34760670 (Allen), National Institutes of Health Grant Nos. R21NS114603 (Allen and Oshinski) and R01EB027774 (Oshinski). Additionally, this material is based upon work supported by the National Science Foundation Graduate Research Fellowship Program under Grant No. 1937971 (El Sayed). Any opinions, findings, and conclusions, or recommendations expressed in this material are those of the author(s) and do not necessarily reflect the views of the National Science Foundation.

Declarations

Conflict of interest The authors declare no conflict or financial interests in this manuscript.

Human, Animal, and Informed Consent No human or animal studies were carried out by the authors of this article.

References

1. Nayak, K. S., J.-F. Nielsen, M. A. Bernstein, et al. Cardiovascular magnetic resonance phase contrast imaging. *J. Cardiovasc. Magn. Reson.* 17(1):71, 2015. <https://doi.org/10.1186/s12968-015-0172-7>.
2. Markl, M., A. Frydrychowicz, S. Kozerke, M. Hope, and O. Wieben. 4D flow MRI. *J. Magn. Reson. Imaging.* 36(5):1015–1036, 2012. <https://doi.org/10.1002/jmri.23632>.
3. Szajer, J., and K. Ho-Shon. A comparison of 4D flow MRI-derived wall shear stress with computational fluid dynamics methods for intracranial aneurysms and carotid bifurcations—a review. *J. Magn. Reson. Imaging.* 48:62–69, 2018. <https://doi.org/10.1016/j.mri.2017.12.005>.
4. Chatzimavroudis, G. P., J. N. Oshinski, R. H. Franch, et al. Evaluation of the precision of magnetic resonance phase velocity mapping for blood flow measurements. *J. Cardiovasc. Magn. Reson.* 3(1):11–19, 2001. <https://doi.org/10.1081/JCMR-100000142>.
5. Nilsson, A., K. M. Bloch, J. Töger, E. Heiberg, and F. Ståhlberg. Accuracy of four-dimensional phase-contrast velocity mapping for blood flow visualizations: a phantom study. *Acta Radiol.* 54(6):663–671, 2013. <https://doi.org/10.1177/0284185113478005>.
6. Montalba, C., J. Urbina, J. Sotelo, et al. Variability of 4D flow parameters when subjected to changes in MRI acquisition parameters using a realistic thoracic aortic phantom. *Magn. Reson. Med.* 79(4):1882–1892, 2018. <https://doi.org/10.1002/mrm.26834>.

7. Zimmermann, J., D. Demedts, H. Mirzaee, et al. Wall shear stress estimation in the aorta: Impact of wall motion, spatiotemporal resolution, and phase noise. *J. Magn. Reson. Imaging*. 2018. <https://doi.org/10.1002/jmri.26007>.
8. Shen, X., S. Schnell, A. J. Barker, et al. Voxel-by-voxel 4D flow MRI-based assessment of regional reverse flow in the aorta. *J. Magn. Reson. Imaging*. 47(5):1276–1286, 2018. <https://doi.org/10.1002/jmri.25862>.
9. Callaghan, F. M., R. Kozor, A. G. Sherrah, et al. Use of multi-velocity encoding 4D flow MRI to improve quantification of flow patterns in the aorta. *J. Magn. Reson. Imaging*. 43(2):352–363, 2016. <https://doi.org/10.1002/jmri.24991>.
10. Garcia, J., A. J. Barker, and M. Markl. The role of imaging of flow patterns by 4D flow MRI in aortic stenosis. *JACC Cardiovasc. Imaging*. 12(2):252–266, 2019. <https://doi.org/10.1016/j.jcmg.2018.10.034>.
11. Puiseux, T., A. Sewonu, O. Meyrignac, et al. Reconciling PC-MRI and CFD: an in-vitro study. *NMR Biomed*. 32(5):e4063, 2019. <https://doi.org/10.1002/nbm.4063>.
12. Kweon, J., D. H. Yang, G. B. Kim, et al. Four-dimensional flow MRI for evaluation of post-stenotic turbulent flow in a phantom: comparison with flowmeter and computational fluid dynamics. *Eur. Radiol*. 26(10):3588–3597, 2016. <https://doi.org/10.1007/s00330-015-4181-6>.
13. Ngo, M. T., C. I. Kim, J. Jung, et al. Four-dimensional flow magnetic resonance imaging for assessment of velocity magnitudes and flow patterns in the human carotid artery bifurcation: comparison with computational fluid dynamics. *Diagnostics*. 9(4):223, 2019. <https://doi.org/10.3390/diagnostics9040223>.
14. Ngo, M. T., U. Y. Lee, H. Ha, et al. Improving blood flow visualization of recirculation regions at carotid bulb in 4D flow MRI using semi-automatic segmentation with ITK-SNAP. *Diagnostics*. 11(10):1890, 2021. <https://doi.org/10.3390/diagnostics11101890>.
15. Roldán-Alzate, A., S. García-Rodríguez, P. V. Anagnostopoulos, et al. Hemodynamic study of TCPC using in vivo and in vitro 4D flow MRI and numerical simulation. *J. Biomech*. 48(7):1325–1330, 2015. <https://doi.org/10.1016/j.jbiomech.2015.03.009>.
16. Edelstein, W. A., M. Mahesh, and J. A. Carrino. MRI: time is dose—and money and versatility. *J. Am. Coll. Radiol*. 7(8):650–652, 2010. <https://doi.org/10.1016/j.jacr.2010.05.002>.
17. Sajed, P. I., J. N. Gonzalez, C. A. Cronin, et al. Carotid bulb webs as a cause of “cryptogenic” ischemic stroke. *AJNR Am. J. Neuroradiol*. 38(7):1399–1404, 2017. <https://doi.org/10.3174/ajnr.A5208>.
18. Haussen, D. C., J. A. Grossberg, S. Koch, et al. Multicenter experience with stenting for symptomatic carotid web. *Intervent. Neurol*. 2018. <https://doi.org/10.1159/000489710>.
19. Haussen, D. C., J. A. Grossberg, M. Bousslama, et al. Carotid web (intimal fibromuscular dysplasia) has high stroke recurrence risk and is amenable to stenting. *Stroke*. 48(11):3134–3137, 2017. <https://doi.org/10.1161/strokeaha.117.019020>.
20. Park, C. C., R. El Sayed, B. B. Risk, et al. Carotid webs produce greater hemodynamic disturbances than atherosclerotic disease: a DSA time–density curve study. *J. Neurointerv. Surg*. 2021. <https://doi.org/10.1136/neurintsurg-2021-017588>.
21. Ozaki, D., T. Endo, H. Suzuki, et al. Carotid web leads to new thrombus formation: computational fluid dynamic analysis coupled with histological evidence. *Acta Neurochir. (Wien)*. 162(10):2583–2588, 2020. <https://doi.org/10.1007/s00701-020-04272-2>.
22. Antonowicz, A., K. Wojtas, Ł. Makowski, W. Orsiuch, and M. Kozłowski. Particle image velocimetry of 3D-printed anatomical blood vascular models affected by atherosclerosis. *Materials*. 16(3):1055, 2023.
23. Ford, M. D., H. N. Nikolov, J. S. Milner, et al. PIV-measured versus CFD-predicted flow dynamics in anatomically realistic cerebral aneurysm models. *J. Biomech. Eng*. 2008. <https://doi.org/10.1115/1.2900724>.
24. Raschi, M., F. Mut, G. Byrne, et al. CFD and PIV analysis of hemodynamics in a growing intracranial aneurysm. *Int. J. Numer. Methods Biomed. Eng*. 28(2):214–228, 2012. <https://doi.org/10.1002/cnm.1459>.
25. Mitsouras, D., T. C. Lee, P. Liacouras, et al. Three-dimensional printing of MRI-visible phantoms and MR image-guided therapy simulation. *Magn. Reson. Med*. 77(2):613–622, 2017. <https://doi.org/10.1002/mrm.26136>.
26. Object30Pro, *Objet30 Pro Key Features: Create parts with the precision, look and feel of real production parts*. <https://www.javelin-tech.com/3d/stratasys-3d-printer/objet30-pro/>.
27. Summers, P. E., D. W. Holdsworth, H. N. Nikolov, B. K. Rutt, and M. Drangova. Multisite trial of MR flow measurement: phantom and protocol design. *J. Magn. Reson. Imaging*. 21(5):620–631, 2005. <https://doi.org/10.1002/jmri.20311>.
28. Wilson, J. S., M. Islam, and J. N. Oshinski. In vitro validation of regional circumferential strain assessment in a phantom aortic model using cine displacement encoding with stimulated echoes MRI. *J. Magn. Reson. Imaging*. 55(6):1773–1784, 2022. <https://doi.org/10.1002/jmri.27972>.
29. Wu, S. P., S. Ringgaard, and E. M. Pedersen. Three-dimensional phase contrast velocity mapping acquisition improves wall shear stress estimation in vivo. *J. Magn. Reson. Imaging*. 22(3):345–351, 2004. <https://doi.org/10.1016/j.mri.2004.01.002>.
30. Markl, M., A. Harloff, T. A. Bley, et al. Time-resolved 3D MR velocity mapping at 3T: improved navigator-gated assessment of vascular anatomy and blood flow. *J. Magn. Reson. Imaging*. 25(4):824–831, 2007. <https://doi.org/10.1002/jmri.20871>.
31. Stalder, A. F., M. F. Russe, A. Frydrychowicz, et al. Quantitative 2D and 3D phase contrast MRI: optimized analysis of blood flow and vessel wall parameters. *Magn. Reson. Med*. 60(5):1218–1231, 2008. <https://doi.org/10.1002/mrm.21778>.
32. Ku, D. N., and D. P. Giddens. Laser Doppler anemometer measurements of pulsatile flow in a model carotid bifurcation. *J. Biomech*. 20:407–421, 1987. [https://doi.org/10.1016/0021-9290\(87\)90048-0](https://doi.org/10.1016/0021-9290(87)90048-0).
33. Ku, D. N., D. P. Giddens, D. J. Phillips, and D. E. Strandness. Hemodynamics of the normal human carotid bifurcation: in vitro and in vivo studies. *Ultrasound. Med. Biol*. 11(1):13–26, 1985. [https://doi.org/10.1016/0301-5629\(85\)90003-1](https://doi.org/10.1016/0301-5629(85)90003-1).
34. Ku, D. N., D. P. Giddens, C. K. Zarins, and S. Glagov. Pulsatile flow and atherosclerosis in the human carotid bifurcation. Positive correlation between plaque location and low oscillating shear stress. *Arteriosclerosis*. 5(3):293–302, 1985. <https://doi.org/10.1161/01.ATV.5.3.293>.
35. Markl, M., F. Wegent, T. Zech, et al. In vivo wall shear stress distribution in the carotid artery. *Circ. Cardiovasc. Imaging*. 3(6):647–655, 2010. <https://doi.org/10.1161/CIRCIMAGING.110.958504>.
36. Frydrychowicz, A., A. Berger, M. F. Russe, et al. Time-resolved magnetic resonance angiography and flow-sensitive 4-dimensional magnetic resonance imaging at 3 Tesla for blood flow and wall shear stress analysis. *J. Thoracic. Cardiovasc. Surg*. 136(2):400–407, 2008. <https://doi.org/10.1016/j.jtcvs.2008.02.062>.
37. Frydrychowicz, A., A. F. Stalder, M. F. Russe, et al. Three-dimensional analysis of segmental wall shear stress in the aorta by flow-sensitive four-dimensional-MRI. *J. Magn. Reson. Imaging*. 30(1):77–84, 2009. <https://doi.org/10.1002/jmri.21790>.
38. Harloff, A., T. Zech, F. Wegent, et al. Comparison of blood flow velocity quantification by 4D flow MR imaging with ultrasound at the carotid bifurcation. *AJNR Am. J. Neuroradiol*. 34(7):1407–1413, 2013. <https://doi.org/10.3174/ajnr.A3419>.
39. Medero, R., C. Hoffman, and A. Roldán-Alzate. Comparison of 4D flow MRI and particle image velocimetry using an in vitro

- carotid bifurcation model. *Ann. Biomed. Eng.* 46(12):2112–2122, 2018. <https://doi.org/10.1007/s10439-018-02109-9>.
40. Cibis, M., W. V. Potters, F. J. Gijsen, et al. The effect of spatial and temporal resolution of cine phase contrast MRI on wall shear stress and oscillatory shear index assessment. *PLoS One.* 11(9):e0163316–e0163316, 2016. <https://doi.org/10.1371/journal.pone.0163316>.
 41. Oktar, S. O., C. Yücel, D. Karaosmanoglu, et al. Blood-flow volume quantification in internal carotid and vertebral arteries: comparison of 3 different ultrasound techniques with phase-contrast MR imaging. *AJNR Am. J. Neuroradiol.* 27(2):363–369, 2006.
 42. Potters, W. V., H. A. Marquering, E. VanBavel, and A. J. Nederveen. Measuring wall shear stress using velocity-encoded MRI. *Curr. Cardiovasc. Imaging Rep.* 7(4):9257, 2014. <https://doi.org/10.1007/s12410-014-9257-1>.
 43. Petersson, S., P. Dyverfeldt, and T. Ebbers. Assessment of the accuracy of MRI wall shear stress estimation using numerical simulations. *J. Magn. Reson. Imaging.* 36(1):128–138, 2012. <https://doi.org/10.1002/jmri.23610>.
 44. Potters, W.V., P. van Ooij, H. Marquering, E. vanBavel, and A.J. Nederveen. *Volumetric arterial wall shear stress calculation based on cine phase contrast MRI.* *J. Magn. Reson. Imaging* 2015 41(2):505–516. <https://doi.org/10.1002/jmri.24560>.
 45. Bae, T., J. H. Ko, and J. Chung. Turbulence intensity as an indicator for ischemic stroke in the carotid web. *World Neurosurg.* 2021. <https://doi.org/10.1016/j.wneu.2021.07.049>.
 46. Choi, P. M. C., D. Singh, A. Trivedi, et al. Carotid webs and recurrent ischemic strokes in the era of CT angiography. *AJNR Am. J. Neuroradiol.* 36(11):2134–2139, 2015. <https://doi.org/10.3174/ajnr.A4431>.
 47. Compagne, K. C. J., K. Dilba, E. J. Postema, et al. Flow patterns in carotid webs: a patient-based computational fluid dynamics study. *AJNR Am. J. Neuroradiol.* 40(4):703–708, 2019. <https://doi.org/10.3174/ajnr.A6012>.
 48. Kumar, D. R., E. Hanlin, I. Glurich, J. J. Mazza, and S. H. Yale. Virchow's contribution to the understanding of thrombosis and cellular biology. *Clin. Med. Res.* 8(3–4):168–172, 2010. <https://doi.org/10.3121/cmr.2009.866>.
 49. Lee, B. K. Computational fluid dynamics in cardiovascular disease. *Korean Circ. J.* 41(8):423–430, 2011. <https://doi.org/10.4070/kcj.2011.41.8.423>.
 50. Iffrig, E., L. H. Timmins, R. El Sayed, W. R. Taylor, and J. N. Oshinski. A new method for quantifying abdominal aortic wall shear stress using phase contrast magnetic resonance imaging and the Womersley solution. *J. Biomech. Eng.* 2022. <https://doi.org/10.1115/1.4054236>.
 51. Katritsis, D., L. Kaiktsis, A. Chaniotis, et al. Wall shear stress: theoretical considerations and methods of measurement. *Prog. Cardiovasc. Dis.* 49(5):307–329, 2007. <https://doi.org/10.1016/j.pcad.2006.11.001>.

Publisher's Note Springer Nature remains neutral with regard to jurisdictional claims in published maps and institutional affiliations.

Springer Nature or its licensor (e.g. a society or other partner) holds exclusive rights to this article under a publishing agreement with the author(s) or other rightsholder(s); author self-archiving of the accepted manuscript version of this article is solely governed by the terms of such publishing agreement and applicable law.

Authors and Affiliations

Retta El Sayed¹  · Alireza Sharif² · Charlie C. Park² · Diogo C. Haussen³ · Jason W. Allen^{1,2,3} · John N. Oshinski^{1,2,3} 

¹ Department of Biomedical Engineering, The Wallace H. Coulter, Emory University and Georgia Institute of Technology, Atlanta, GA, USA

² Department of Radiology & Imaging Sciences, Emory University, 1364 Clifton Rd, Atlanta, GA 30322, USA

³ Department of Neurology, Emory University, Atlanta, GA, USA